

The effects of MAPK activity on cell-cell adhesion during wound healing

John T. Nardini^a, Douglas A. Chapnick^b, Xuedong Liu^b, David. M. Bortz^{*a}

^a*Department of Applied Mathematics, University of Colorado, Boulder, CO, United States 80309-0526*

^b*Department of Chemistry and Biochemistry, University of Colorado, Boulder, CO, United States 80303-0596.*

Abstract

The mechanisms underlying *collective migration*, or the coordinated movement of a population of cells, are not well understood despite its ubiquitous nature. As a means to investigate collective migration, we consider a wound healing scenario in which a population of cells fills in the empty space left from a scratch wound. Here we present a simplified mathematical model that uses reaction-diffusion equations to model collective migration during wound healing with an emphasis on cell movement and its response to both cell signaling and cell-cell adhesion. We use the model to investigate the effect of the MAPK signaling cascade on cell-cell adhesion during wound healing after EGF treatment. Our results suggest that activation of the MAPK signaling cascade stimulates collective migration through increases in the pulling strength of leader cells. We further use the model to suggest that treating a cell population with EGF converts the time to wound closure (as function of wound area) from parabolic to linear.

Keywords: Collective Migration, Cell signaling, Reaction-Diffusion Equations, Wound healing, Epithelial-to-Mesenchymal Transition

1. Introduction

Collective migration, or the coordinated movement of a population of cells is a ubiquitous biological process involved in tissue formation and repair, developmental regulation, and tumorigenesis [40]. Although there has been a heavy focus on collective migration in recent scientific literature, the mechanisms underlying this important process are still not well understood [4, 6, 12, 34]. Determining the underlying mechanisms behind collective migration behavior will likely provide insight into wound healing, as well as the epithelial-to-mesenchymal transition (EMT) and metastasis characteristics of tumor progression during cancer [7].

Significant intercellular communication is required for a group of cells to coordinate their movement as one unit during collective migration. Recent studies have sought to understand how activation of the mitogen-activated protein kinase (MAPK) signaling cascade may promote collective migration [6, 21]. The MAPK signaling cascade affects many cellular activities, ranging from cellular migration to angiogenesis [21, 31, 34, 43, 47, 48]. While several types of MAPKs appear to influence cell migration, the extracellular signal-regulated kinas 1/2 (ERK) MAPKs are dominant regulators of cellular migration. ERK influences cellular migration in a variety of cell types and is

*Corresponding author D.M. Bortz

Email address: dmbortz@colorado.edu (David. M. Bortz*)

downstream from the epidermal growth factor receptor (EGFR) [23, 27, 46]. EGFR is a tyrosine kinase receptor that forms an active dimer state in the presence of ligand, and its main ligand is epidermal growth factor (EGF). Receptor dimerization initiates autophosphorylation of the intracellular EGFR tyrosine kinase domains, which recruit signal transducers, such as the Ras protein. These transducers then trigger various intracellular signaling cascades, most notably the MAPK and ERK signaling cascades [19, 48]. Accordingly, we focus on the activation of ERK in response to EGF treatment in this study.

Collective migration is defined by three main characteristics: physical and functional connection between cells, multicellular polarity, and the deposition and remodeling of the extracellular matrix [12]. We focus on the first of these hallmarks through cell-cell adhesion. We also note, however, that many aspects of *single* cell migration, such as molecular control of protrusions, polarity, shape generation, and cell-surface adhesion also affect collective migration [10, 13, 20, 32, 36]. Cell-cell adhesion is believed to have a stronger influence on collective migration than these aforementioned single cell features, yet its role is still poorly understood. [12, 13]. For this reason, we ignore the effects of cell-surface adhesion and focus on cell-cell adhesion, as has been done in previous studies on collective migration [1, 24, 44, 45].

Adherens junctions mediate cell-cell adhesion in tissues by attaching actin and intermediate filament cytoskeletons between adjacent cells, thereby allowing for dynamic coordinate force transmission between the actin cytoskeletons of physically contacting cells [12]. Adherens junctions form between cells through transmembrane cadherin proteins, which bind actin filaments through zyxin, vinculin, and α -catenin adapter proteins [16, 26]. Cadherin proteins have been reported as both promoters and inhibitors of cell migration, so their overall role is not clear [12, 14, 18, 35]. Based on this uncertainty in the role of cell-cell junctions during collective migration and the MAPK cascade's well-established (stimulating) role [6, 21, 31, 34], we pose the following question: how does MAPK activity influence the main role of cell-cell junctions during collective migration?

To provide insight into collective migration, we will concentrate on wound healing induced in a sheet of cells from the human keratinocyte (HaCaT) cell line. Experiments, as previously described in [6], are conducted in which a wound comprised of open space is formed in a monolayer of cells by scratching away a portion of the population with a pipette tip. The remaining cell population begins a collective migration process into the wound and eventually fills in and closes the wound. Studies of this sort tend to split cells in the population into two distinct classifications: leader cells (those located at the wound interface) and follower cells (those located farther away from the wound). We use live-cell imaging to capture the cell profiles over time (every half hour) for 30 hours and analyze both untreated (denoted as *mock*) and EGF-treated cell populations to analyze the effects of both EGF and the MAPK signaling cascade on collective migration.

Mathematical models can provide insight into how EGF treatment stimulates collective migration, which may be difficult to decipher through experimental procedures. Some authors strongly advocate for mathematical models as necessary for a comprehensive understanding of signaling cascades due to their complex quantitative nature

[8]. Accordingly, we focus on developing a simple first mathematical model to investigate the relationship between collective migration, the MAPK cascade, and cell-cell adhesion. In particular, we will develop two models to investigate how the MAPK signaling cascade affects cell-cell adhesion in response to EGF treatment during wound healing.

Other studies have used various quantitative approaches to model collective migration. A partial differential equation (PDE)-based model is advantageous for modeling collective migration, as it allows for an in-depth analysis of the biological system paired with the ability to search for certain patterns, such as traveling wave solutions to the model [9, 17]. This class of wave solutions frequently arise in models of biological systems [20, 29, 39] as well as in collective migration models due their ability to capture invasive wave front dynamics¹ [30, 33]. Fisher’s equation (originally used to model the spread of advantageous genes [11]) is the classical example of a PDE model with traveling wave solutions, and it has been used previously to model collective migration in response to the wounding of a human peritoneal mesothelial cell population [30].

A more recent study developed a two-dimensional continuum model based on the force of lamellipodia, cell-substrate adhesion, and cell-cell adhesion that can reproduce results from both contraction experiments of enterocytes and expansion experiments of Madin-Darby canine kidney (MDCK) cells [3]. A later study demonstrated that simulations from this model also matched the leading edge velocity of experimental data in intestinal enterocyte (IEC) cells [2]. This model was further used as a means to identify the effects of wound shape and area on the time for wound closure. Ultimately, the authors concluded that the rate of change of the wound area during wound healing is likely proportional to the square root or first power of the wound area in IEC cells. This was an improvement over previous studies that assumed the rate of change of the wound area is constant, which yielded inaccurate estimates for larger wounds [15].

In [38], the authors computationally recreated the results of [34], in which two waves of MAPK activation were observed in MDCK cells during wound healing. The authors of [38] developed a four-species PDE model for MAPK activation during wound healing that can quantitatively recapitulate these two MAPK activation waves. The components of this model include an arbitrary diffusible ligand (such as EGF), its cell-surface receptor, an intracellular precursor to this ligand, and reactive oxygen species. This study ignored cell migration, however, and thus did not investigate the effect of these waves on wound healing. Other previous PDE models have focused on how cell signaling effects cell migration. In [42], the authors showed how one simple regulatory chemical (impacting only cell proliferation) is sufficient for a simple reaction-diffusion model to match data on wound healing of epidermal cells.

In this study, we will develop two testable PDE models using reaction-diffusion equations in order to elucidate properties of the interaction between MAPK signaling, cellular migration, and cell-cell adhesion in a wounded

¹Discrete random walk models have also been proposed to model collective migration and can yield similar mean-field results to PDE models [4, 37].

HaCaT cell population in response to EGF treatment. These models will aid in making predictions on cellular migration in epithelial cell populations.

We use these two models to test two competing hypotheses regarding the influence of MAPK activation on the role of cell-cell adhesion during wound healing. The first hypothesis states that *MAPK activity stimulates collective migration through decreases in the drag strength of follower cells*. We denote the corresponding mathematical model as Model H since cell-cell adhesion will *hinder* migration. The second hypothesis states that *MAPK activity stimulates collective migration through increases in the pulling strength of leader cells*. We denote the corresponding mathematical model as Model P since cell-cell adhesion will *promote* migration. While both models are able to fit leading edge data, we demonstrate that the model based on the second hypothesis can better match various characteristics of the cell population during wound healing. These model results suggest that the dominant role of cell-cell adhesion in response to MAPK activation after EGF treatment is to promote leader cell pulling rather than inhibit the drag of follower cells.

In Section 2, we present our two model derivations based on the above hypotheses. In Section 3, we demonstrate how Model P can match the leading edge dynamics better than Model H and then use Model P to predict wound closure as a function of wound area in HaCaT cell populations. Lastly, in Section 4, we conclude with a discussion on the implications of these results as well as plans for future work.

2. Model Development

Our mathematical models presented here consist of two coupled variables describing cell density, $u(t, x)$, and the average cellular MAPK activation level, $m(t)$, where our independent variables include time (t) and spatial location (x). While we are investigating cell-cell interactions in this study, current techniques cannot directly measure these interactions. Hence, we use cell density as a means to investigate cell-cell interactions during migration, because it is measurable and indicative of physical interaction, so high cell densities should display a larger degree of cell-cell interaction effects on migration. We include the diffusion of cells and focus on its response to different levels of MAPK activity. This can be quantitatively described using a conservation law framework as:

$$u_t(t, x) = \nabla \cdot (f_u^D \nabla u), \quad m_t(t) = f_m^A, \quad (2.1)$$

where the subscript t denotes differentiation with respect to time, f_u^D denotes the rate of cellular diffusion and f_m^A describes the activation rate of $m(t)$. It should be noted that cell proliferation and death could be included in Equation (2.1), but are assumed negligible over the course of the experiment². Decreases in MAPK activation could also be considered in Equation (2.1), however, we do not see any noticeable decreases in MAPK levels during EGF experiments, so we exclude them as well. Note that while we simulate our model in only one spatial dimension due

²The inclusion of a growth term had a minimal effect on model simulations and hypothesis evaluation (results not presented in this work).

to the one-dimensional plane wave-behavior in the wound healing data, the model can be easily extended to two or three dimensions.

We will develop two different models in Section 2.1: Model H focuses on how cell movement towards the wound may be hindered by the drag of follower cells, while Model P focuses on how leader cells may pull on cells behind them to promote movement towards the wound. While we generally think of follower and leader cells in terms of their location in the population, we assume that each cell behind the first row in our population will either pull on those behind it or hinder those in front of it. The resulting models thus distinguish the dominant interaction (dragging or pulling) between neighboring cells in the population during wound healing.

In the rest of this section, we describe the development of two simple models for different hypotheses on the emergence of collective migration during wound healing. In Section 2.1.1, we describe our first diffusion term in which cell-cell adhesions hinder motion, while in Section 2.1.2, we describe a different diffusion model where cell-cell adhesions promote motion. Section 2.2 details our assumptions on MAPK activation in response to EGF treatment. In Section 2.3, we then combine the models from Sections 2.1.1 and 2.1.2 with the observations on MAPK activation in Section 2.2 to describe our models for EGF data in Sections 2.3.1 and 2.3.2, respectively. We then detail the entire model, including initial and boundary conditions, in Section 2.4 and outline our parameter estimation procedure in Section 2.5.

2.1. Models for diffusion

In this section, we will derive two different models (Models H and P) for diffusion based off cell-cell adhesion. In order to do so, we first discretize our solution domain. We use a uniform grid for both the time and space domain, so the time interval may be denoted as $t(j) = j\Delta t$, $j = 0, \dots, N - 1$, where N denotes the total number of time points used, and $x(i) = i\Delta x$, $i = 0, \dots, M - 1$ where M denotes the number of spatial points used. We simplify notation by writing $t(j) = t_j$, $x(i) = x_i$, and write our discretized solution as $u(t_j, x_i) = u_i^j$.

2.1.1. Model H: cell-cell adhesions hinder migration

For our first model on the effects of cell-cell adhesion on diffusion, we assume that cell-cell adhesions *hinder* migration through the drag of follower cells and accordingly denote it as Model H. In this scenario, the downregulation of cell-cell adhesions will promote migration. We create this model by modifying a previous cell migration study that incorporates cell-cell adhesion.

In [1], the authors developed a mathematical model that assumes cell-cell adhesions hinder cell movement. To derive the model, a probability transition τ_i^+ is given for a cell density located at position x_i attempting to move forward to location x_{i+1} by

$$\tau_i^+ = \frac{(1 - u_{i+1})(1 - \alpha u_{i-1})}{\Delta x^2} \quad (2.2)$$

where the first factor represents space filling (e.g., the cell density is more likely to move forward given a smaller

cell density in front of it). The parameter α denotes the (dimensionless) rate of cell-cell adhesion, and thus *the second term in Equation (2.2) represents our first hypothesis in which follower cells (denoted with u_{i-1}) hinder the movement of cells in front of them towards the wound*. The transition probabilities τ_{i-1}^+ , τ_i^- , and τ_{i+1}^- are all defined analogously (with the minus signs denoting cells moving backwards). We note that Equation (2.2) may be modified to include the influence of other aspects of cell migration, including cell-surface adhesion and shape change [13].

Given these transition probabilities, Anguige and Schmeiser derive the continuum limit of the model by analyzing the change of cell density u_i over time as

$$u_t = \tau_{i-1}^+ u_{i-1} + \tau_{i+1}^- u_{i+1} - (\tau_i^+ + \tau_i^-) u_i \quad (2.3)$$

and then taking the limit as $\Delta x \rightarrow 0$. The derivation of the continuum limit of Equation (2.3) is presented in [1] and may be written as the dimensionless model

$$u_t = ((1 + 3\alpha(u - 2/3)^2 - 4/3\alpha)u_x)_x,$$

and we accordingly write the dimensional model as

$$u_t = ((D + 3\gamma(u - 2/3)^2 - 4/3\gamma)u_x)_x. \quad (\text{Model H}) \quad (2.4)$$

In Equation (2.4), D and γ denote the rates of diffusion and cell-cell adhesion with units $\text{microns}^2/\text{hr}$. Hence the diffusion rate for Model H is

$$f_u^D = D + 3\gamma(u - 2/3)^2 - 4/3\gamma.$$

We note that backwards diffusion may occur with Equation (2.4) if $4\gamma > 3D$ and address this inequality more after final model development in Section 2.3.1.

2.1.2. Model P: cell-cell adhesions promote migration

For our second model, we assume that cell-cell adhesions *promote* migration as leader cells pull the cells behind them forward and denote it as Model P. In this scenario, the upregulation of cell-cell adhesion will promote migration. We now denote the forward transition probability τ_i^+ of cell density u_i as

$$\tau_i^+ = \frac{(1 - u_{i+1})(1 + \alpha u_{i+1})}{\Delta x^2}, \quad (2.5)$$

where the first term again represent space filling, but *the second term in Equation (2.5) represents our second assumption in which leader cells (denoted with u_{i+1}) promote movement towards the wound by pulling on the cells behind them.* We note again that τ_{i-1}^+ , τ_i^- , and τ_{i+1}^- are all defined analogously. Substituting the transition probability from Equation (2.5) into Equation (2.3) yields

$$\begin{aligned}
u_t &= \frac{(1-u_i)(1+\alpha u_i)u_{i-1} + (1-u_i)(1+\alpha u_i)u_{i+1} - ((1-u_{i+1})(1+\alpha u_{i+1}) + (1-u_{i-1})(1+\alpha u_{i-1}))u_i}{\Delta x^2} \\
&= \frac{u_{i-1} + \alpha u_{i-1}^2 u_i - \alpha u_{i-1} u_i^2 + u_{i+1} - 2u_i - \alpha u_i^2 u_{i+1} + \alpha u_i u_{i+1}^2}{\Delta x^2} \\
&= \frac{u_{i-1} - 2u_i + u_{i+1}}{\Delta x^2} + \alpha \frac{u_{i-1}^2 u_i - u_{i-1} u_i^2 - u_i^2 u_{i+1} + u_i u_{i+1}^2}{\Delta x^2}, \tag{2.6}
\end{aligned}$$

where we can recognize the first term on the right hand side as the standard central difference approximation to the second derivative. For the second term on the right hand side, we can simplify using Taylor series approximations as: $u_{i+1} \approx u_i + \Delta x \cdot u_i' + \Delta x^2/2 \cdot u_i''$, $u_{i-1} \approx u_i - \Delta x \cdot u_i' + \Delta x^2/2 \cdot u_i''$, where primes denote a spatial derivative term. Substituting these terms into the second term on the right hand side of Equation (2.6) reveals

$$\begin{aligned}
u_t &= \frac{u_{i-1} - 2u_i + u_{i+1}}{\Delta x^2} + \alpha \frac{2\Delta x^2 u_i (u_i')^2 + u_i^2 u_i'' \Delta x^2 + \mathcal{O}(\Delta x^4)}{\Delta x^2} \\
&= u_i'' + \alpha(2u_i (u_i')^2 + u_i^2 u_i'') + \mathcal{O}(\Delta x^2) \\
&= u_i'' + \alpha(u_i^2 u_i')' + \mathcal{O}(\Delta x^2)
\end{aligned}$$

resulting in the dimensionless continuum limit to be

$$u_t = ((1 + \alpha u^2)u_x)_x,$$

which we dimensionalize as

$$u_t = ((D + \gamma u^2)u_x)_x, \quad (\text{Model P}) \tag{2.7}$$

where D and γ again denote the dimensionalized rates of cell diffusion and cell-cell adhesion, respectively. Thus the rate of diffusion for Model P is given as

$$f_u^D = D + \gamma u^2.$$

We note that a more general form of this equation has been used previously to model temperature fronts and can have traveling wave solutions under certain scenarios [41].

2.2. MAPK activation and cell growth in response to EGF treatment

While we have difficulty matching experimental data over the entire experiment, our models performed well in the time range of 10 hours after EGF treatment until the end of the experiment at $t = 30$ hours. In Figure 2.1, we

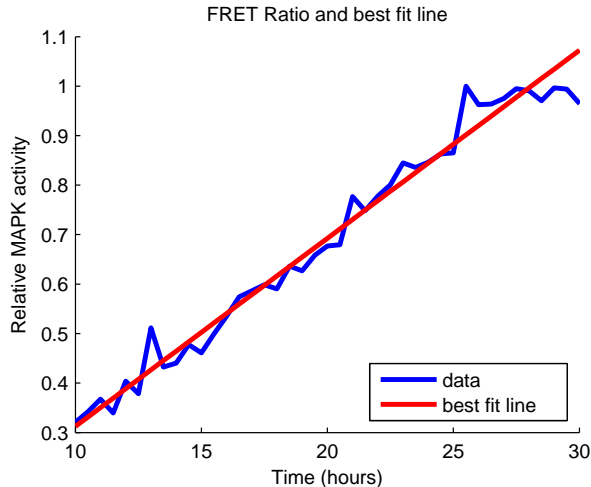


Figure 2.1: Plotting the relative average FRET ratio of the cell population during the EGF experiment from $t = 10$ to 30 hours, along with its best fit line, which is given by $b(t)$ in the text. Note that this data has an R^2 value of 0.98.

have plotted the normalized average level of FRET ratio (indicative of MAPK activation in the population) during the experimental protocol. The activation levels after $t = 10$ appear linear, so we focus on matching data in this time interval ($t = 10 - 30$ hours) and use a linear term for MAPK activation. We have plotted a best-fit line to the normalized FRET ratio data from $t = 10 - 30$ hours in Figure 2.1, which is given by $b(t) = -0.0675 + 0.0380t$. Note that this data has an R^2 value of 0.98 to help justify this linear term. We thus set f_m^A as a constant, c , in Equation (2.1). Also note that $b(t) > 1$ after $t \approx 28$ hours, even though the data has been normalized, so we set $m(t) = 1$ for these values.

2.3. Models for EGF data

We now present the final models for collective migration in response to EGF treatment. We do so by assuming that the rate of cell-cell adhesion changes over time in response to the level of m activation. This requires a variable term, denoted by $\Gamma(m)$, instead of a constant value, γ , for the rate of cell-cell adhesion.

2.3.1. Model H: MAPK stimulates collective migration through decreases in drag strength

To conclude Model H, we now extend f_u^D in Equation (2.4) to include changes in cell-cell adhesion in response to different levels of MAPK activation. This model is consistent with the hypothesis that *MAPK activity stimulates collective migration through decreases in the drag strength of follower cells*. We use a linear cell-cell adhesion term as a function of MAPK activity, m , by $\Gamma(m) = \gamma(1 - m)$, for some cell-cell adhesion constant $\gamma > 0$. Note that $0 \leq m \leq 1$ so that $\Gamma(m) \geq 0$.

Accordingly, our final description for Model H in response to EGF treatment is given by

$$u_t(t, x) = ((D + 3\Gamma(m)(u - 2/3)^2 - 4/3\Gamma(m))u_x)_x, \quad m_t(t) = c \quad (\text{Model H for EGF}) \quad (2.8)$$

where $\Gamma(m)$ is given above. We note that if $4D < 3\Gamma(m)$, the above equation will exhibit backwards diffusion, which is not well-defined. Fortunately, all parameter sets in this study do not satisfy this inequality for the entirety of the simulation.

2.3.2. Model P: MAPK activation stimulates collective migration by increases in pulling strength

We extend f_u^D from Equation (2.7) to include changes in cell-cell adhesion in response to different levels of MAPK activation for Model P in response to EGF data. In this scenario, we assume that *MAPK activity stimulates collective migration through increases in the pulling strength of leader cells*. Accordingly, we model the cell-cell adhesion level as a function of m by $\Gamma(m) = \gamma m$, for some constant γ . As a result, Model P for EGF-treated cells is given by

$$u_t(t, x) = ((D + \Gamma(m)u^2)u_x)_x + ku(1 - u), \quad m_t(t) = c, \quad (\text{Model P for EGF}) \quad (2.9)$$

where $\Gamma(m)$ is given above.

2.4. Complete models, initial and boundary conditions

We've now introduced the two models under consideration in this study. We briefly review the two models, along with their terms and assumptions in Table 1. A list of all parameters used throughout this study is also given in Table 2.

Model features	H		P	
Cell-cell adhesions	Hinder migration		Promote migration	
Simulation	mock	EGF	mock	EGF
Equation	(2.4)	(2.8)	(2.7)	(2.9)
MAPK impact on cell-cell adhesions	n/a	Downregulation	n/a	Upregulation
$\Gamma(m)$	γ	$\gamma(1 - m)$	γ	γm

Table 1: Summary of equations and assumptions used for Models H and P.

If we let w denote the location of the wound, then we would ideally use an initial condition that is nonzero for all $x \leq w$ to imitate the presence of cells and zero for all $x > w$ to imitate the wound. Scratching the cell population with the pipette tip, however, initially shocks the cells and causes slow initial movement. For this reason, we use a nonzero initial condition for all $x \leq \tilde{w} = w - 180$ microns and a zero initial condition for all $x > \tilde{w}$. This alteration to the initial condition allows us to match the wave phenomena of both the model and data. We compute the nonzero portion of the initial condition by interpolating the data profile at the initial time point. Thus, our initial

Parameter	Description (units)	Model H		Model P		Determined by
		Mock	EGF	Mock	EGF	
D	Baseline rate of diffusion (microns ² /hr)	19,770	177,940	2.19	0.14	Fitting
c	Rate of MAPK activation (hr ⁻¹)	0	0.038	0	.038	$b(t)$
γ	Rate of adhesion between adjacent cells (microns ² /hr) for mock (microns ² /hr·m) for EGF	1.68	970	30,614	535,810	Fitting
w	Location of wound (microns)	1550	1620	1550	1620	From data

Table 2: List of parameters for the models, along with the parameter values used and how we obtained these values.

condition is given by

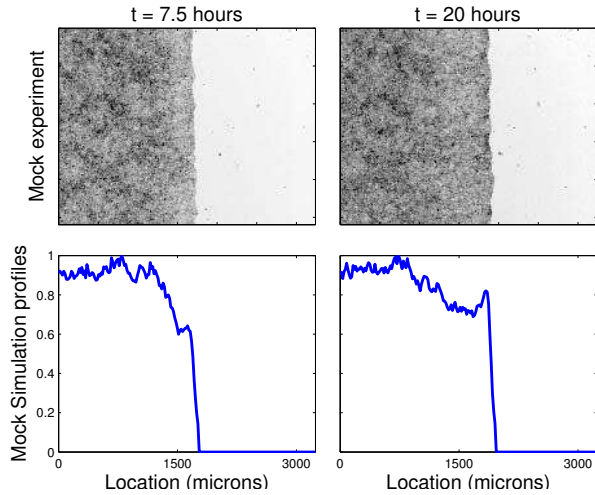
$$\begin{aligned}
u(t_0, x) &= \begin{cases} \psi(x); & x \leq \tilde{w} \\ 0; & \text{otherwise} \end{cases} \\
m(t_0) &= b(t_0).
\end{aligned} \tag{2.10}$$

where t_0 is our starting time for simulations (e.g., $t_0 = 10$ hours) and ψ denotes the interpolated, normalized initial data profile values at time t_0 . In Figure 2.2, we've included some typical video snapshots at $t = 7.5, 20$ hours, along with their resulting density profile. In order to obtain this population profile from data, we sum over the vertical axis for each image matrix and then normalize over each time step. The linear interpolation of this initial profile (at $t = t_0$) is our $\psi(x)$ function used for the initial condition. Because of the linear MAPK activation phase between $t = 10 - 30$ hours, we will simulate the model from $t = 7.5$ to 30 hours, where we also run the model for an extra 2.5 hours due to its initial high speeds. We also include the leading edge locations of the two experiments in the bottom portion of Figure 2.2, whose calculation is described in the following section.

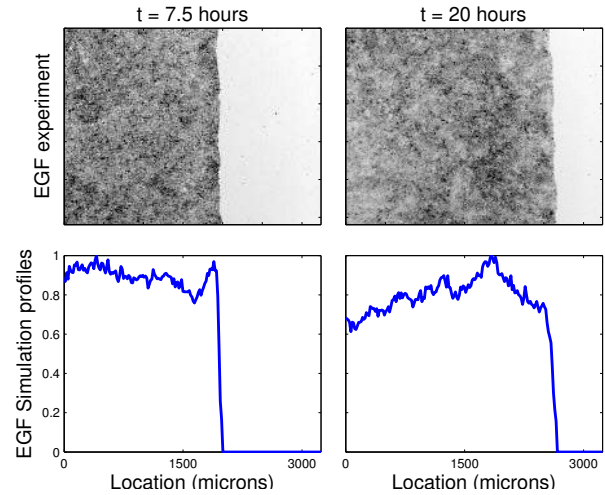
We use zero Neumann boundary conditions to simulate no flux conditions at the walls of the well plate. Note that in experimental videos, we only observe a $3.24 \text{ mm} \times 3.24 \text{ mm}$ field of view, whereas the experimental domain is actually 7 mm long and 5 mm wide, so there is plenty of space for the cells to move in either direction. Accordingly, we extend our computational domain 1.62 mm behind the field of view and 3.24 mm in front of the field of view to ensure the boundaries do not affect the model simulations.

2.5. Parameter estimation

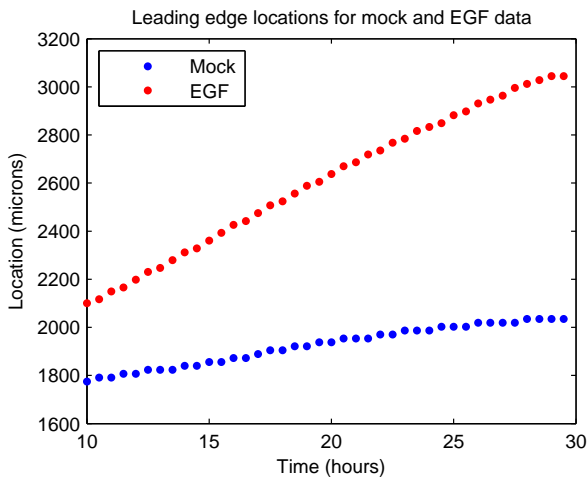
In order to fit our model simulations to data on wound healing, we will use an inverse problem procedure to estimate the parameter vector $\vec{q} = [D, \alpha]^T$ for both models for both mock and EGF data. We do so by comparing



(a) Experimental snap shots of the experiment and resulting profiles for the mock experiments. Top row: Images of the wound healing experiment at $t = 7.5$ and 20 hours. Bottom row: Resulting profiles for the cell population in the image.



(b) Experimental snap shots of the experiment and resulting profiles for the EGF experiments. Top row: Images of the wound healing experiment at $t = 7.5$ and 20 hours. Bottom row: Resulting profiles for the cell population in the image.



(c) Locations of the mock (blue) and EGF (red) experimental leading edges over time using Equation (2.11), which identifies the first point where $u(t_j, x_i) \leq 0.3$ for each time point t_j , as is described in Section 2.5. Note that the mock leading edge data may take the same value for several consecutive time points because it moves slowly, and the camera discretizes the experimental domain.

Figure 2.2

the locations of the leading edge for both the experimental data and model simulations, as has been done in previous studies on wound healing [25, 30]. In this work, we will define the leading edge as the location in which the relative density is equal to a certain value, although we note that it has different definitions elsewhere [6]. As seen in Figures 3.3 and 3.4, a density of 0.3 can locate the leading edge well. Accordingly, we define $\ell_{m,0.3}(t, \hat{q})$ as the leading edge location over time for the model using \hat{q} as an estimate for the true \vec{q} , denoted by

$$\ell_{m,0.3}(t, \hat{q}) = \{x | u(x, t) = 0.3, \vec{q} = \hat{q}\}.$$

Note that with numerical computations, we cannot precisely estimate the leading edge in this manner. Accordingly, we estimate the leading edge to be the first location where the relative density is below the set threshold. For instance, if $\ell_{m,0.3}^n(\hat{q})$ denotes the leading edge location at time t_n , then we approximate it as:

$$\ell_{m,0.3}^n(\hat{q}) \approx \hat{\ell}_{m,0.3}^n(\hat{q}) = \{x_i | u_i^n \leq 0.3 \text{ and } u_k^n > 0.3 \text{ for all } k < i, \vec{q} = \hat{q}\}. \quad (2.11)$$

We use analogous definition for the estimate of the leading edge of the normalized data over time, which is denoted as $\hat{\ell}_{D,0.3}^n$.

As a means to estimate \vec{q} using our models, we will implement an inverse problem in which we minimize a cost function [5]. In this work, we will use the cost function given by an ordinary least squares estimate:

$$J(\vec{q}) = \sum_{n=1}^N |\hat{\ell}_{m,0.3}^n(\vec{q}) - \hat{\ell}_{D,0.3}^n|^2,$$

where N is the number of time points considered. To find the value of \vec{q} that minimizes the cost function, we use the Nelder-Mead algorithm as implemented in MATLAB's `fminsearch` command.

3. Results

To investigate the performance of Models H and P in describing the wound healing process, we now compare both models to mock and EGF experimental data. To compare these prediction to the experimentally determined results, we use images of the cell populations over time, such as those depicted in Figure 2.2. We use several different criteria for comparison to the experimental data. In Section 3.1, we compare the leading edge locations of the model simulations and experimental data for both of the mock and EGF cases. In Section 3.2, we compare the wave speed values of the EGF model simulations to the experimental data wave speed values. In Section 3.3, we directly compare the experimental snapshots to the model profiles over time. We conclude the results section by using Model P to investigate the time to wound closure as a function of the wound area in Section 3.4.

3.1. Leading edge fitting

Using the protocol described in Section 2.5, we fit both models to both mock and EGF data. The resulting leading edge simulations are depicted in Figure 3.1, and the parameters used to obtain these plots are given in Table 2. The red dots in Figure 3.1 represent the location of the experimental leading edge over time, while the green and blue lines represent the leading edge locations for Models H and P, respectively. The thin black dash-dot lines represent one standard deviation of the data, and we describe their computation in the appendix. Note that the scale for the two images is very different, as the leading edge in EGF simulations moves much faster and farther than the leading edge in mock simulations. Recall that mock leading edge data sometimes takes the same value for several consecutive time points because it moves slowly, and the camera discretizes the experimental domain.

In the mock simulations (depicted in the left image of Figure 3.1), both models appear to match the leading edge data in a similar manner. In particular, after $t = 18$ hours, the two leading edge simulations appear superimposed, suggesting that these two very different models can yield similar results for predicting the the leading edge location. Table 2 summarizes, however, that these two models use very different simulations to obtain these similar results. Note that Model H relies primarily on diffusion for movement, as it uses a large baseline diffusion constant of $D = 19,770$ microns²/hr, compared to Model P, which uses a much smaller value of $D = 2.19$ microns²/hr. On the other hand, Model P uses a large rate of cell-cell adhesion, as it estimates $\gamma = 30,614$ microns²/hr while Model H estimates $\gamma = 1.68$ microns²/hr for its rate of cell-cell adhesion. Thus we see that Model H uses a high rate of diffusion to match the mock data, whereas Model P uses a high rate of cell-cell adhesion to match this data. These results are not surprising based on the derivations of these two models, as cell-cell adhesions hinder movement for Model H but promote movement for Model P.

Extending the same parameter estimation methodology to EGF data, we see on the right hand side of Figure 3.1 that Model P fits the experimental data better than Model H. Model P matches the experimental data well at the initial time point of $t = 10$ hours and continues to do so until the final time point. On the other hand, Model H initially overestimates the leading edge from $t = 10 - 20$ hours (so much so that it even fails to match the data to within one standard deviation at times) and then underestimates the leading edge location from $t = 20 - 30$ hours. We thus observe that Model H is unable to accurately simulate the EGF data, suggesting that MAPK activation may not decrease drag strength during wound healing when the cell population is treated with EGF.

Looking at the parameter values for Model P simulations in Table 2, we see that the estimate for γ increases significantly in response to EGF treatment. More surprising, however, is the decrease in the rate of baseline cell diffusion that we observe between the mock and EGF simulations for Model P, from $D = 2.19$ microns²/hr in the mock experiment to $D = 0.14$ microns²/hr in the EGF experiment. Due to the relative insensitivity of Model P to the parameter D (results not shown), we can likely consider these values of D as equivalent. Hence, MAPK activation appears to have a negligible effect on the baseline rate of diffusion. This is an interesting observation, as one may initially suspect that increases in MAPK activation increase the baseline rate of diffusion as a means to

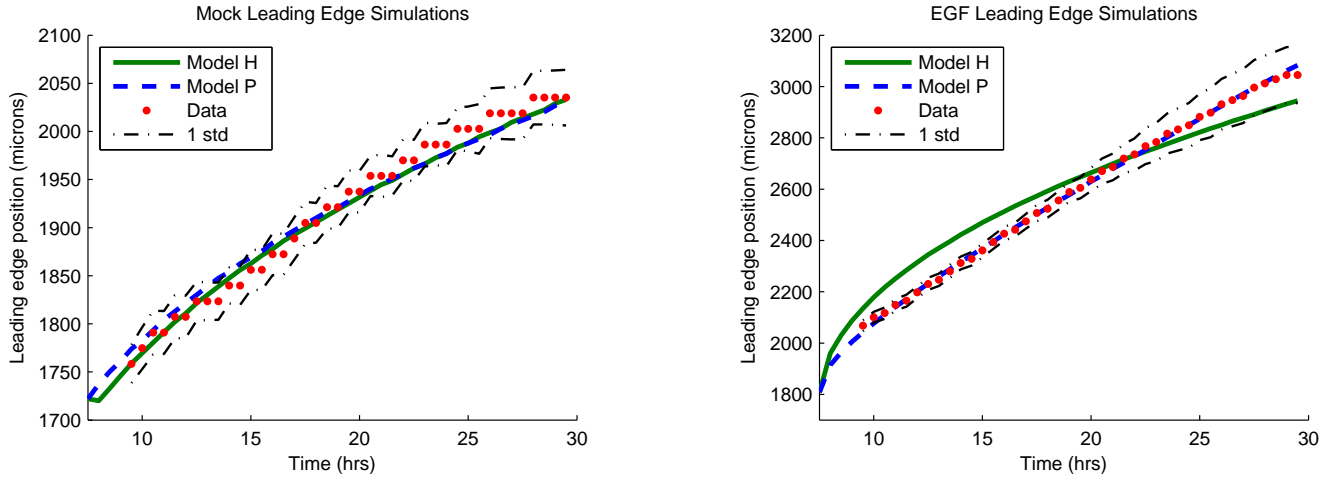


Figure 3.1: Leading edge simulations for both mock- (left) and EGF- (right) treated cell populations. The red dots represent the experimental leading edge locations over time, and the solid green and dashed blue lines represent the leading edge locations for Models H and P, respectively. Note that while both models can match the mock data relatively well, model P appears to fit EGF data better than model H. The black dash-dot lines denote one standard deviation of the leading edge locations, and their computation is described in the appendix.

stimulate migration, as we observe for Model H, whose estimates of D change from 19,770 to 177,940 microns/hr² in response to EGF treatment.

3.2. Wave speed comparisons

A previous study on predicting the time for wound closure in intestinal epithelial cells used instantaneous velocity of the wound edge to compare model simulations with experimental data [2]. In a similar fashion, we compare wave speed simulations of both the experimental data and the best-fit model simulations from the previous section. We use a forward difference calculation on the leading edge locations over time to estimate the model simulation wave speeds, $w_{m,\beta}^n$, for various normalized cellular density levels (given by $\beta = 0.2, 0.3, 0.4$):

$$w_{m,\beta}^n = \frac{\tilde{\ell}_{m,\beta}^{n+1} - \tilde{\ell}_{m,\beta}^n}{\Delta t},$$

and the data wave speeds are calculated analogously. In this equation, $\tilde{\ell}_{m,\beta}^n$ denotes the 4-point moving average (computed using MATLAB's smooth function) of the leading edge location at time t_n using β as the leading edge threshold. We use $\tilde{\ell}_{m,\beta}^n$ instead of $\hat{\ell}_{m,\beta}^n$ in this calculation to obtain realistic wave speed values. Note that the data has a very sharp front, which causes similar wave speed values for all densities considered from $t = 10 - 20$ hours, which is demonstrated in Figure 3.2b.

The results for EGF scenario model and data wave speeds for $\beta = 0.2, 0.3, 0.4$ are depicted in Figure 3.2a in green, blue, and red, respectively. Note that both model wave speeds appear to have two different behavior phases: an initial fast phase (likely due to the presence of empty space), followed by a sustained, slowly decreasing phase.

The previous study also observed these two phases of behavior and sometimes also observed an increase in speed towards the end of the simulation due to wound closure. Compare these changes in phase behavior with that of the the data, which initially has a constant velocity but begins to slow down after $t = 20$ hours. The initial high velocity of the model simulations (and lack thereof in the experimental data) is why we let the model simulations run for 2.5 hours before comparing their leading edges with the experiments.

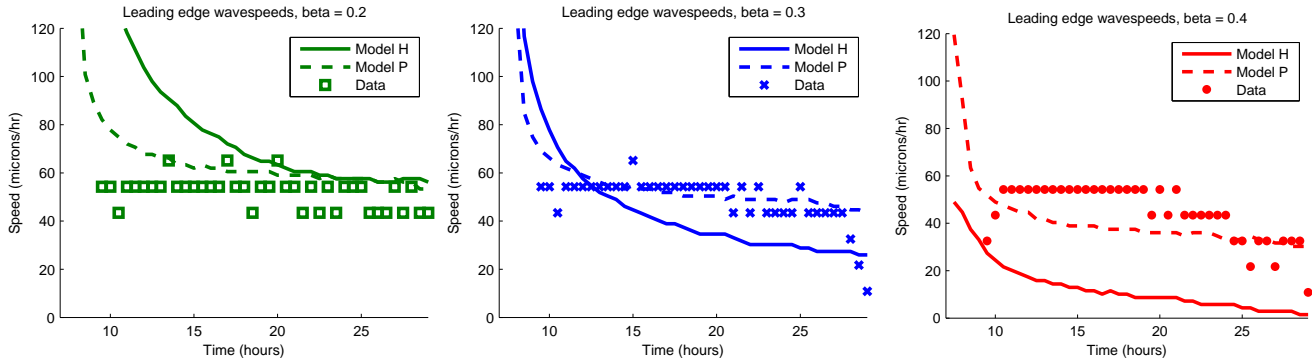
In comparing the two models' wave speed simulations to the data, we see that Model H consistently underestimates the wave speed for $\beta = 0.3, 0.4$, and overestimates the wave speed for $\beta = 0.2$. On the other hand, Model P can match the faster phase of the data for $\beta = 0.2$ (around 55 microns/hr) from $t = 17 - 30$ hours, and the slower phases of the data (between 35 and 45 microns/hr) for $\beta = 0.3$ and $\beta = 0.4$ from $t = 20 - 29$ hours. Overall, Model P tends to match the data better than Model H for all time points. In Figure 3.2b, we superimpose all data and model wave speed values to obtain a better picture of the overall population wave speeds. Here we again observe more agreement between the experimental data and Model P than we observe for Model H. From these simulations, it is not surprising that Model P can more accurately fit the leading edge data than Model H, as its best-fit simulation better matches the wave speeds of the data.

3.3. Comparison to data snap shots

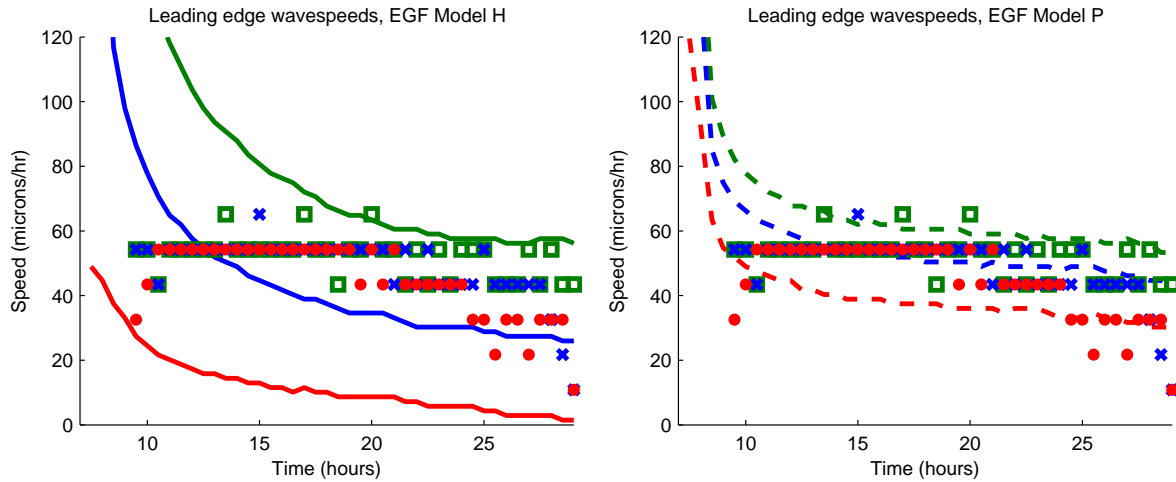
We next compare the model profiles to experimental snapshots over time for both mock and EGF simulations. These images are depicted in Figures 3.3 and 3.4 for mock and EGF data, respectively, for $t = 10, 17.5, 25,$ and 29.5 hours. In each snapshot, the top frame represents the experimental image of the cell sheet during the wound healing experiment, and the bottom frame demonstrates the model simulations for both Models H and P. In each snapshot, the experimental leading edge is depicted with a black line in the top frame and a black dot in the bottom frame.

In Figure 3.3, we note that both Models H and P match the experimental leading edge well, as we would expect from Figure 3.1. However, the two resulting profiles are very different, as Model H has a gradually decreasing profile in comparison to the steep population front of Model P. Considering our previous observation that Model H uses a high rate of diffusion to match the leading edge, whereas Model H uses a high rate of cell-cell adhesion, these two different model profiles are not surprising. Note that this gradually descending cell profile causes Model H to predict a significant presence of cells in locations that are clearly empty in the experiment. For example, at $t = 29.5$ hours, Model H predicts a cellular density of about $u(t = 29.5, x = 2500) = 0.25$ (one quarter of the maximum cellular density at $x = 2500$ microns), whereas the experimental cell sheet has clearly not yet reached this location, and its leading edge is approximately 500 microns further back. We believe this difference in profile front descent allows Model P to better predict the leading edge location and various wave speeds of the experimental wound healing data.

Figure 3.4 depicts the same figure for the EGF experiments and simulations. We again notice that both profiles tend to agree near the leading edge location, but yield very different profile simulations. Model H's profile again



(a) Wave speed comparisons for EGF scenarios for Model H (solid line), Model P (dashed line), and experimental data (various shapes). The wavespeeds for $\beta = 0.2$ are compared in green, for $\beta = 0.3$ are in blue, and for $\beta = 0.4$ are in red. Note that model P tends to match the data better than Model H, and that Model H consistently over and underestimates almost all wave speed values from the data for $\beta = 0.2$ and $\beta = 0.4$, respectively.



(b) Superposition of all density wave speeds with data. Model H is depicted on the left hand side, and Model P is depicted on the right hand side. Note that Model P agrees more with the data than Model H.

Figure 3.2: Wave speed simulations for the two models in comparison with data.

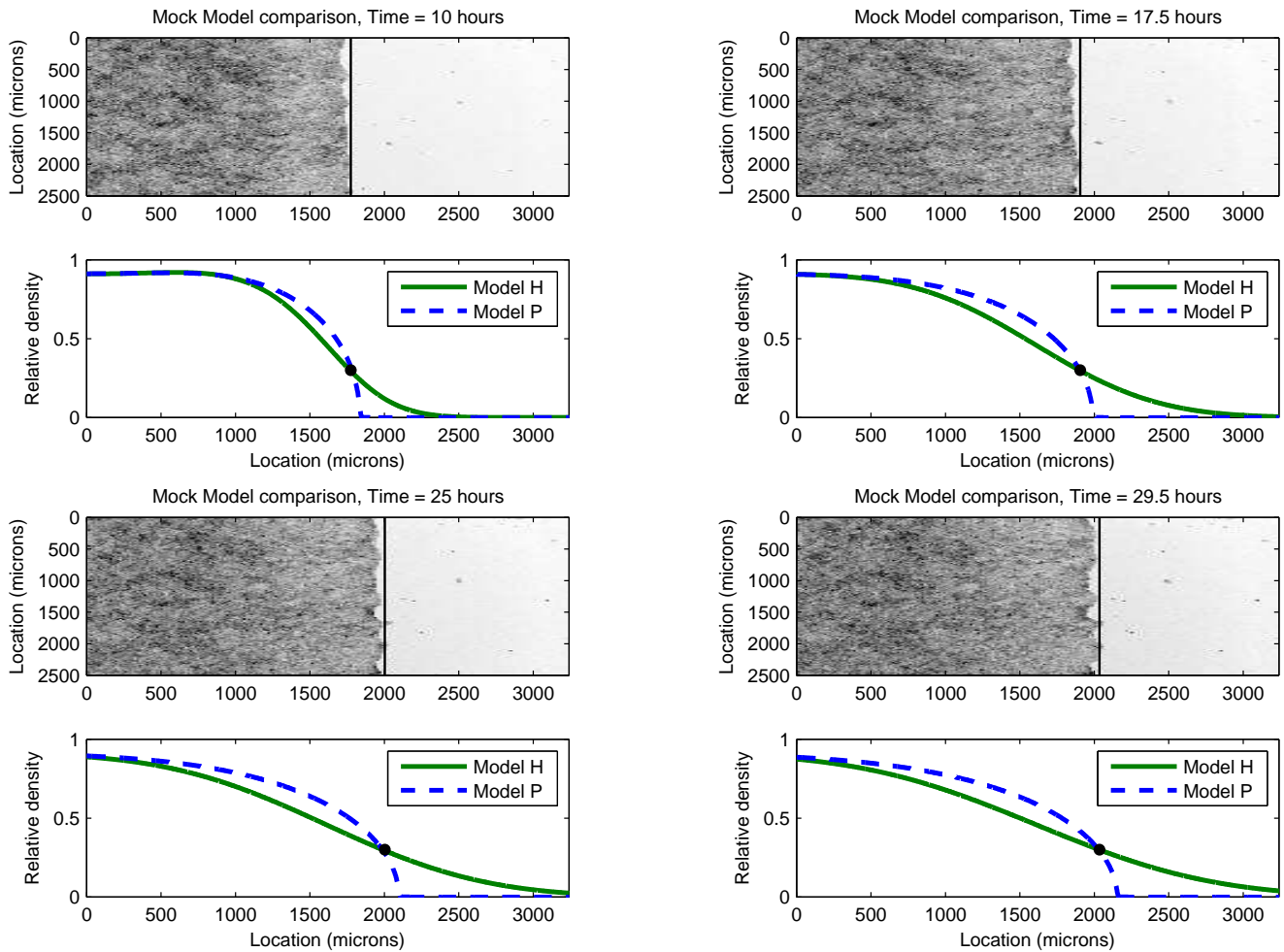


Figure 3.3: Comparisons of experimental images (upper frames) to model profiles (lower frames) for the mock experiments over various time snapshots. The black line in the upper frames and dot in the bottom frames depict the experimental leading edge over time. Note the gradually decreasing cell front of Model H in comparison to the sharp front of Model P.

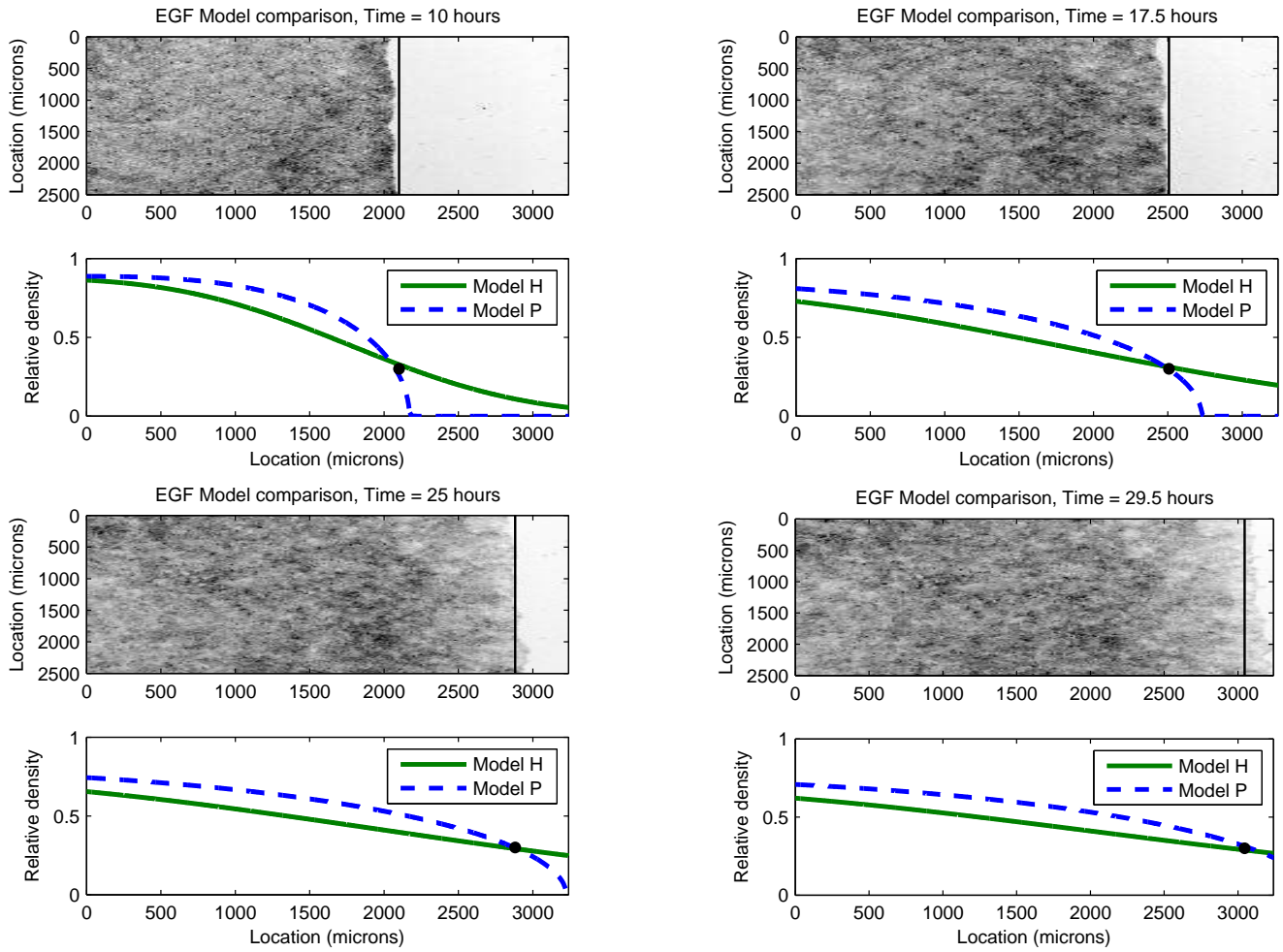


Figure 3.4: Comparisons of experimental images (upper frames) to model profiles (lower frames) for the EGF experiments over various time snapshots. The black line in the upper frames and dot in the bottom frames depict the experimental leading edge over time. Note the gradually decreasing cell front of Model H in comparison to the sharp front of Model P. Observe how this gradual population frony causes Model H to predict a nonzero value for $u(t = 17.5, x = 3000)$, even though there are no cells present at this time and location in the experiment.

descends much more gradually than the steep front of Model P. Similarly, Model H also predicts the presence of cells in areas that are clearly empty in the experimental snapshot, such as at $x = 3000$ microns at $t = 17.5$ hours. We note, however, that Model P also predicts the presence of cells in clearly empty areas from the EGF experiment (such as past $x = 3000$ microns at $t = 25$ hours). This suggests that more sophisticated modeling endeavors are still needed in the future to better capture the leading edge dynamics and match the experimental profiles of wound healing data. Overall, however, Model P can accurately match the leading edge dynamics well for both mock and EGF simulations, whereas Model H is considerably flawed in several aspects. These results support our second hypothesis that *MAPK activation in response to EGF treatment stimulates collective migration by increasing the pulling strength of leader cells.*

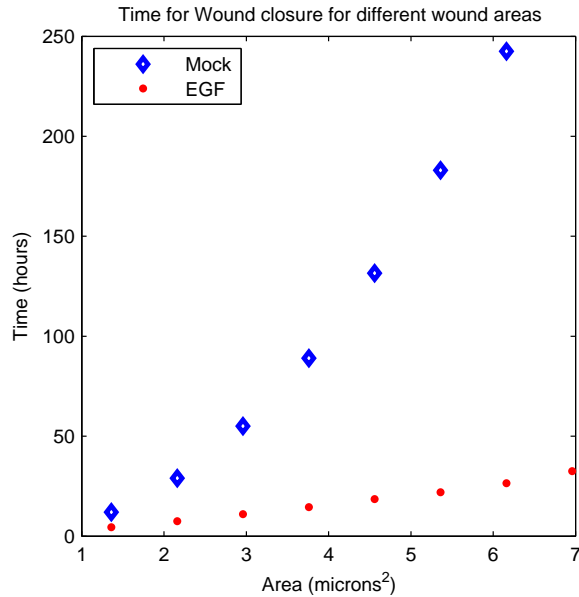


Figure 3.5: Using Model P to predict the time to wound closure as a function of wound area. The blue diamonds denote closure time for mock cells, whereas the red dots denote closure time for EGF-treated cells. Note that the time to wound closure for mock-treated cells appears quadratic, which matches results from [2]. The time to wound closure appears to become linear in response to EGF treatment.

3.4. Time to wound closure

A common theme in wound healing studies is to investigate how different wound aspects, including size, shape, and aspect ratio, affect the time to wound closure [2, 15]. Times for wound closure as a function of wound area were analyzed in [2] for different wound shapes and sizes. In a similar fashion, we can use Model P to predict the closure times for various different wound sizes, as is depicted in Figure 3.5. Because this model is simulated in one dimension, we only use it on rectangular wound shapes, where we calculate the wound area by multiplying the length of the wound by the width of the well (4 microns). We also define the time to wound closure as the time it takes for the leading edge to reach the end of the field of view (3,240 microns), or t_k such that $\hat{\ell}_{m,0.3}^k = 3,240$ microns. Notice in this figure how the time to wound closure for mock cells appears approximately quadratic, which would be consistent with [2], in which the authors suggested that the rate of change of wound area is proportional to the area of the wound in IEC cells. In response to EGF treatment, however, we see this curve change to a much faster and apparently linear term. We can validate these predicted times in future studies by experimenting with wounds of various sizes. We may also investigate nonrectangular wounds in the future by extending our model to two dimensions.

4. Conclusions and Discussion

In this study, we have developed two mathematical models representing the spread of a cellular sheet during wound healing in response to EGF treatment. These two models are used to test two hypotheses on the effects of

MAPK activity on cell-cell adhesion during collective migration. Model H assumes that MAPK activity stimulates collective migration through decreases in the drag strength of follower cells, whereas Model P assumes that MAPK activity stimulates collective migration through increases in the pulling strength of leader cells. Model P matches several aspects of the experimental data better than Model H, ultimately suggesting the validity of our second hypothesis. From our resulting parameter values, we also observe that the main effect of MAPK activity on cell migration is an increase in the rate of cell-cell adhesion, and that it has a negligible effect on the baseline rate of diffusion. As one may initially suspect that increases in MAPK activation stimulate the baseline rate of diffusion to promote the rate of migration, we plan to further investigate this observation in future experimental and computational studies due to its nonintuitive nature

These conclusions have implications in our understanding of the EMT, in which cells detach from an epithelial cell population as mesenchymal cells [7, 12]. Cells undergoing EMT tend to gain migratory and invasive properties, and hence the EMT is a driving factor in both normal embryological development and cancer metastasis [7, 22]. There are two main types of EMT: incomplete and complete. During incomplete EMT, cell-cell junctions remain intact between certain invasive cells, and collective strand-like migration is observed. Complete EMT is characterized by the loss of most cell connections, and individual cells detach from the population to begin their own migration pattern. Hence, in either form of EMT, we see that cells detach from the population and can be considered smaller cell subpopulations (Composed of one or several cells), effectively increasing the prevalence of leader cells. Since cell pulling appears to be the dominant mechanism of collective migration, we suggest that HaCaT cells in response to EGF treatment may express incomplete EMT behaviors so that an increased number of leader cells can effectively guide smaller cell subpopulations via pulling. We may use this observation to better understand incomplete EMT dynamics through the experimental system and mathematical analysis, along with an understanding of any possible connections between incomplete and complete EMT. For example, if any sort of chemical treatment or oncogenic perturbations will convert the system from incomplete to complete EMT or vice versa.

In Figure 4.1, we have depicted several data and model contours over time. From these contours, we see that Model P is able to accurately match the leading edge data for both mock and EGF data, but it is still far from matching the entire data profile accurately over time. Future endeavors will aim to match the entire population profile instead of just the leading edge. We note that the role that the MAPK signaling cascade on cell-surface adhesion during collective migration is another important question that requires investigation. Further exploration into this may aid in better matching the entire cell population profile. We also note that we used a simple linear term for average MAPK activation levels in our model. The slope of this line very likely depends on the amount of EGF treatment in the population, however, so future studies will include more sophisticated modeling terms that may involve EGF ligand, its intracellular precursor, and reactive oxygen species, as has been done in a previous model on MAPK activation during wound healing[38]. EGF ligand secretion by leader cells likely aids in collective

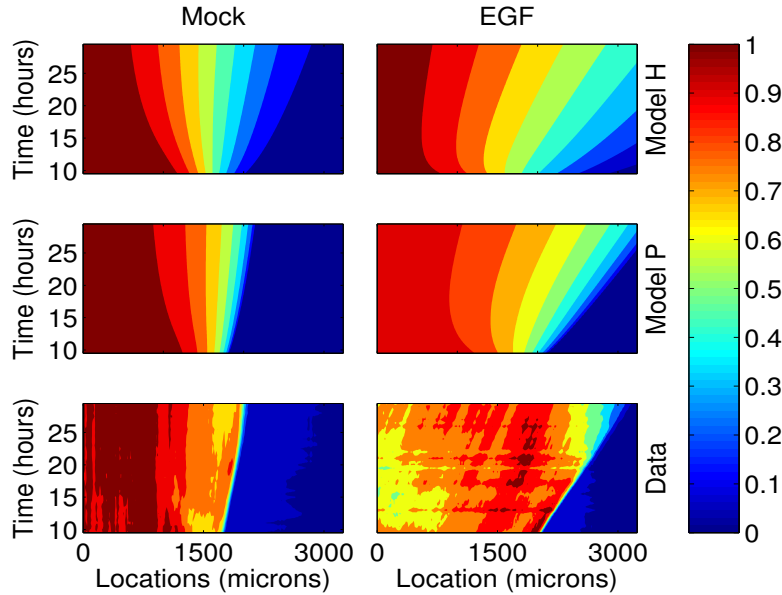


Figure 4.1: Contours for the two models (top two rows) against data (bottom row). The x -axis depicts the spatial location and the y -axis depicts time to demonstrate how the profiles change over time for both model simulations and the actual experiment. The colorbar depicts the cellular density levels (i.e., blue denotes a low density and red denotes a high density).

migration as ligand diffusion to follower cells will further promoting cell pulling in the population.

In this work, we have developed a simple model to investigate how EGF treatment influences collective migration during wound healing in HaCaT cells. We demonstrate that cell-cell adhesion plays a critical and activating role in collective migration through leader cell pulling. This model may have implications in understanding EMT dynamics, including how cells may transition from incomplete to complete EMT and vice versa.

Acknowledgements

JTN is supported by the Interdisciplinary Quantitative Biology (IQ Biology) program at the BioFrontiers Institute, University of Colorado, Boulder, which is supported by NSF IGERT grant number 1144807. This work was in part supported by grants from National Institutes of Health R01CA107098 to X.L. The authors would like to thank Joe Dragavon and the BioFrontiers Advanced Light Microscopy Core for their microscopy support. The ImageXpress MicroXL was supported by a NCRR grant S10 RR026680 from the NIH.

Appendix

Numerical implementation

Note that for numerical implementation, we use a method of lines approach with MATLAB's ode15s function to simulate the entire model. For spatial discretization, we use the second order scheme for convection-diffusion

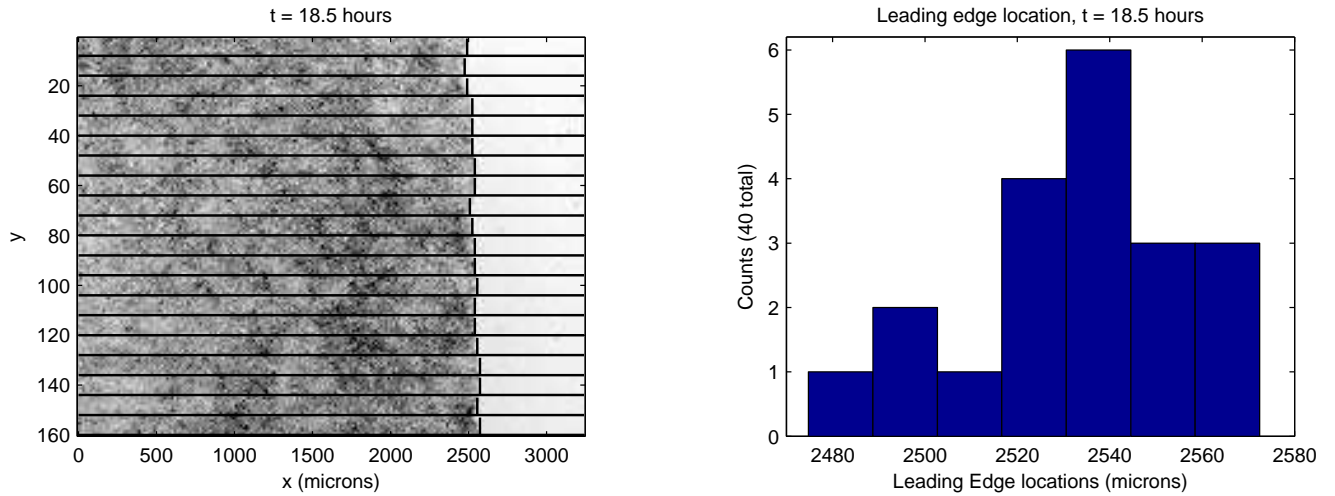


Figure 4.2: Splitting up the y -axis into twenty bins and obtaining several estimates for the leading edge. On the left hand image, we've demonstrated how we split up the axis to calculate several different leading edge locations (denoted by black vertical lines). On the right hand image, we show the histogram of the leading edge locations of the left hand image .

equations (without convection in our case) from [28] given by

$$\dot{u}_j(t) = \frac{P_{j+1/2}(t) - P_{j-1/2}(t)}{\Delta x}$$

where $P_{j+1/2}(t)$ is an approximation to the diffusive flux, given by

$$P_{j+1/2}(t) = \frac{1}{2} \left[Q \left(u_j(t), \frac{u_{j+1}(t) - u_j(t)}{\Delta x} \right) + Q \left(u_{j+1}(t), \frac{u_{j+1}(t) - u_j(t)}{\Delta x} \right) \right]$$

where $Q(u, u_x)$ denotes the cellular diffusion rate. Simulations not shown demonstrate quick convergence in our simulations.

Computing standard deviations

In order to compute the standard deviation of the location of the leading edge at each time point, we split the y -axis of each image into R bins, and compute the leading edge for each of the separate bins to obtain R estimates of the leading edge location in the population. In Figure 4.2, for example, we've split the y -axis into twenty separate bins on the right hand side and calculated the leading edge of the data for each one. Hence, for each time point during the experiment, we compute the sample mean of the leading edge locations (call it $\hat{\mu}$) then compute the sample standard deviation to obtain one standard deviation. On the right side of Figure 4.2, we've also depicted an example histogram for the leading edge locations when using twenty bins.

References

- [1] Anguige, K. and Schmeiser, C. (2009). A one-dimensional model of cell diffusion and aggregation, incorporating volume filling and cell-to-cell adhesion. *J. Math. Biol.*, 58(3):395–427.
- [2] Arciero, J. C., Mi, Q., Branca, M., Hackam, D., and Swigon, D. (2013). Using a continuum model to predict closure time of gaps in intestinal epithelial cell layers. *Wound Repair Regen.*, 21(2):256–65.
- [3] Arciero, J. C., Mi, Q., Branca, M. F., Hackam, D. J., and Swigon, D. (2011). Continuum model of collective cell migration in wound healing and colony expansion. *Biophys. J.*, 100(3):535–43.
- [4] Baker, R. E. and Simpson, M. J. (2012). Models of collective cell motion for cell populations with different aspect ratio: Diffusion, proliferation and travelling waves. *Phys. A Stat. Mech. its Appl.*, 391(14):3729–3750.
- [5] Banks, H. T. Tran, H. (2009). *Mathematical and Experimental Modeling of Physical and Biological Processes*. CRC Press, Boca Raton, Florida New York.
- [6] Chapnick, D. A. and Liu, X. (2014). Leader cell positioning drives wound-directed collective migration in TGF β -stimulated epithelial sheets. *Mol. Biol. Cell*, 25(10):1586–93.
- [7] Chapnick, D. A., Warner, L., Bernet, J., Rao, T., and Liu, X. (2011). Partners in crime: the TGF β and MAPK pathways in cancer progression. *Cell Biosci.*, 1(1):42.
- [8] Clarke, D. C. and Liu, X. (2008). Decoding the quantitative nature of TGF-beta/Smad signaling. *Trends Cell Biol.*, 18(9):430–42.
- [9] Curtis, C. W. and Bortz, D. M. (2012). Propagation of fronts in the Fisher-Kolmogorov equation with spatially varying diffusion. *Phys. Rev. E*, 86(6):066108.
- [10] DiMilla, P. A., Barbee, K., and Lauffenburger, D. A. (1991). Mathematical model for the effects of adhesion and mechanics on cell migration speed. *Biophys. J.*, 15(1):15–37.
- [11] Fisher, R. A. (1937). The wave of advance of advantageous genes. *Ann. Eugen.*, 7(4):355–369.
- [12] Friedl, P. and Gilmour, D. (2009). Collective cell migration in morphogenesis, regeneration and cancer. *Nat.Rev.Mol.Cell Bio.*, 10:445–457.
- [13] Friedl, P. and Wolf, K. (2010). Plasticity of cell migration: a multiscale tuning model. *J. Cell Biol.*, 188(1):11–9.
- [14] Geisbrecht, E. R. and Montell, D. J. (2002). Myosin VI is required for E-cadherin-mediated border cell migration. *Nat. Cell Biol.*, 4(8):616–20.

- [15] Gilman, T. (2004). Wound outcomes: the utility of surface measures. *Int. J. Low. Extrem. Wounds*, 3(3):125–32.
- [16] Haley, J. and Gullick, W. (2009). *EGFR signaling networks in cancer therapy*. Humana Press.
- [17] Hammond, J. F. and Bortz, D. M. (2011). Analytical solutions to Fisher’s equation with time-variable coefficients. *Appl. Math. Comput.*, 218(6):2497–2508.
- [18] Hazan, R., Phillips, G., and Qiao, R. (2000). Exogenous expression of N-cadherin in breast cancer cells induces cell migration, invasion, and metastasis. *J. Cell Biol.*, 148(4):779–790.
- [19] Herbst, R. S. (2004). Review of epidermal growth factor receptor biology. *Int. J. Radiat. Oncol. Biol. Phys.*, 59(2):21–6.
- [20] Holmes, W. R., Carlsson, A. E., and Edelstein-Keshet, L. (2012). Regimes of wave type patterning driven by refractory actin feedback: transition from static polarization to dynamic wave behaviour. *Phys. Biol.*, 9(4):046005.
- [21] Huang, C., Jacobson, K., and Schaller, M. D. (2004). MAP kinases and cell migration. *J. Cell Sci.*, 117(Pt 20):4619–28.
- [22] Janda, E., Lehmann, K., Killisch, I., Jechlinger, M., Herzig, M., Downward, J., Beug, H., and Grünert, S. (2002). Ras and TGF β cooperatively regulate epithelial cell plasticity and metastasis: dissection of Ras signaling pathways. *J. Cell Biol.*, 156(2):299–313.
- [23] Jo, M., Thomas, K. S., Somlyo, A. V., Somlyo, A. P., and Gonias, S. L. (2002). Cooperativity between the Ras-ERK and Rho-Rho kinase pathways in urokinase-type plasminogen activator-stimulated cell migration. *J. Biol. Chem.*, 277(14):12479–85.
- [24] Johnston, S. T., Simpson, M. J., and Baker, R. E. (2012). Mean-field descriptions of collective migration with strong adhesion. *Phys. Rev. E*, 85(5):051922.
- [25] Johnston, S. T., Simpson, M. J., and McElwain, D. S. (2014). How much information can be obtained from tracking the position of the leading edge in a scratch assay? *J. R. Soc. Interface*, (May).
- [26] Juliano, R. (2002). Signal transduction by cell adhesion receptors and the cytoskeleton: functions of integrins, cadherins, selectins, and immunoglobulin-superfamily members. *Annu. Rev. Pharmacol. Toxicol.*, pages 283–323.
- [27] Klemke, R. L., Cai, S., Giannini, A. L., Gallagher, P. J., de Lanerolle, P., and Cheresch, D. A. (1997). Regulation of cell motility by mitogen-activated protein kinase. *J. Cell Biol.*, 137(2):481–92.
- [28] Kurganov, A. and Tadmor, E. (2000). New High-Resolution Central Schemes for Nonlinear Conservation Laws and Convection-Diffusion Equations. *J. Comput. Phys.*, 160(1):241–282.

- [29] Langebrake, J. B., Dilanji, G. E., Hagen, S. J., and De Leenheer, P. (2014). Traveling waves in response to a diffusing quorum sensing signal in spatially-extended bacterial colonies. *J. Theor. Biol.*, 363:53–61.
- [30] Maini, P. K., McElwain, D. L. S., and Leavesley, D. I. (2004). Traveling wave model to interpret a wound-healing cell migration assay for human peritoneal mesothelial cells. *Tissue Eng.*, 10(3-4):475–82.
- [31] Matsubayashi, Y., Ebisuya, M., Honjoh, S., and Nishida, E. (2004). ERK Activation Propagates in Epithelial Cell Sheets and Regulates Their Migration during Wound Healing. 14:731–735.
- [32] Mori, Y., Jilkine, A., and Edelstein-Keshet, L. (2008). Wave-pinning and cell polarity from a bistable reaction-diffusion system. *Biophys. J.*, 94(9):3684–97.
- [33] Murray, J. D. (2001). *Mathematical Biology I: An Introduction*, volume 17 of *Interdisciplinary Applied Math.* Springer-Verlag, New York, NY, 3rd edition.
- [34] Nikolić, D. L., Boettiger, A. N., Bar-Sagi, D., Carbeck, J. D., and Shvartsman, S. Y. (2006). Role of boundary conditions in an experimental model of epithelial wound healing. *Am. J. Physiol. Cell Physiol.*, 291(1):C68–75.
- [35] Omelchenko, T. and Hall, A. (2012). Myosin-IXA regulates collective epithelial cell migration by targeting RhoGAP activity to cell-cell junctions. *Curr. Biol.*, 22(4):278–88.
- [36] Palecek, S., Loftus, J., Ginsberg, M., Lauffenburger, D. A., and Horwitz, A. (1997). Integrin-ligand binding properties govern cell migration speed through cell-substratum adhesiveness. *Nature*, 385:537–540.
- [37] Plank, M. J. and Simpson, M. J. (2013). Lattice-free models of cell invasion: discrete simulations and travelling waves. *Bull. Math. Biol.*, 75(11):2150–66.
- [38] Posta, F. and Chou, T. (2010). A mathematical model of intercellular signaling during epithelial wound healing. *J. Theor. Biol.*, 266(1):70–8.
- [39] Roques, L., Garnier, J., Hamel, F., and Klein, E. K. (2012). Allee effect promotes diversity in traveling waves of colonization. *Proc. Natl. Acad. Sci. U. S. A.*
- [40] Rorth, P. (2009). Collective cell migration. *Annu. Rev. Cell Dev. Biol.*, 25:407–29.
- [41] Samarskii, A. A. and Sobol, I. M. (1963). Examples of the numerical calculation of temperature waves. *Zh. vych. mat.*, 3(4):945–970.
- [42] Sherratt, J. A. and Murray, J. D. (1990). Models of epidermal wound healing. *Proc. Biol. Sci.*, 241(1300):29–36.
- [43] Shin, E. Y., Kim, S. Y., and Kim, E. G. (2001). c-Jun N-terminal kinase is involved in motility of endothelial cell. *Exp. Mol. Med.*, 33(4):276–83.

- [44] Thompson, R. N., Yates, C. A., and Baker, R. E. (2012). Modelling Cell Migration and Adhesion During Development. *Bull. Math. Biol.*, 74(12):2793–2809.
- [45] Tremel, A., Cai, A., Tirtaatmadja, N., Hughes, B., Stevens, G., Landman, K., and O’ Connor, A. (2009). Cell migration and proliferation during monolayer formation and wound healing. *Chem. Eng. Sci.*, 64(2):247–253.
- [46] Webb, D. J., Nguyen, D. H. D., and Gonias, S. L. (2000). Extracellular signal-regulated kinase functions in the urokinase receptor- dependent pathway by which neutralization of low density lipoprotein receptor-related protein promotes fibrosarcoma cell migration and Matrigel invasion. *J. Cell Sci.*, 134:123–134.
- [47] Yang, Z., Yang, H., Jiang, Z., Huang, X., Li, H., Li, A., and Cheng, R. (2013). A new method for calculation of flocculation kinetics combining Smoluchowski model with fractal theory. *Colloids Surfaces A Physicochem. Eng. Asp.*, 423:11–19.
- [48] Yewale, C., Baradia, D., Vhora, I., Patil, S., and Misra, A. (2013). Epidermal growth factor receptor targeting in cancer: a review of trends and strategies. *Biomaterials*, 34:8690–8707.